Journal of Materials Science & Technology 253 (2026) 246–257

Contents lists available at ScienceDirect

Journal of Materials Science & Technology

journal homepage: www.elsevier.com/locate/jmst

Research Article

Surface driving stress-assisted rapid and large area silver porous sheet bonding for power electronics packaging

Chuantong Chen[a,*], Luobin Zhang[a,b], Fupeng Huo[a], Minoru Ueshima[c], Yutai Su[d], Xu Long[d], Koji S Nakayama[a], Masahiko Nishijima[a], Hiroaki Miyake[e], Mingyu Li[b], Katsuaki Suganuma[a]

[a] Institute of Scientific and Industrial Research (SANKEN), Osaka University, 8-1, Mihogaoka, Osaka 567-0047, Ibaraki, Japan
[b] Sauvage Laboratory for Smart Materials, School of Materials Science and Engineering, Harbin Institute of Technology (Shenzhen), Shenzhen 518055, China
[c] Daicel Corporation, Grand Front Osaka Tower-B, 3-1, Ofuka-cho, Kita-ku, Osaka 530-0011, Japan
[d] School of Mechanics, Civil Engineering and Architecture, Northwestern Polytechnical University, Xi'an 710129, China
[e] Measurement and Electric Machine Control Laboratory, Tokyo City University, 1-28-1 Tamazutsumi, Setagaya-ku, Tokyo 158-8557, Japan

ARTICLE INFO

Article history:
Received 17 January 2025
Revised 28 July 2025
Accepted 28 July 2025
Available online 21 August 2025

Keywords:
Rapid bonding
Ag porous sheet
High dislocation density
Large area bonding
Solid-state bonding
SiC power modules

ABSTRACT

This study introduces a novel rapid die attach and large-area substrate bonding technology based on an Ag porous sheet with ultra-fine grain structure and surface-driven stress. The Ag porous sheet is fabricated using Ag particles with a high dislocation density, processed via a hot-pressing method without the addition of any organic solvents. The high dislocation density of the Ag particles promotes neck growth during the fabrication of the Ag porous sheet. Additionally, surface polishing alters the grain structure to ultra-fine grains, which generates surface-driven stress. A shear strength of 82.1 MPa was achieved for the SiC dummy chip/Cu substrate joint using this Ag porous sheet, with a bonding time of only 1 min at 250 °C. Furthermore, large-area (30 mm × 30 mm) Cu die-to-Cu substrate bonding was successfully achieved using the Ag porous sheet, with a short heating time of 3 min at 250 °C. The bonding interface exhibited a bonding ratio of over 85 % for the large-area bonding. The rapid bonding mechanism was discussed and analyzed based on the surface stress and grain structure of the Ag porous sheet, validated through electron backscatter diffraction (EBSD) and transmission electron microscopy (TEM), and finite element analysis (FEA). The use of this Ag porous sheet offers a highly efficient process with significant potential for a wide range of SiC power device applications in high-temperature and high-power electronics.

1. Introduction

With the rapid development of microelectronics to meet the increasing demand for wide-bandgap (WBG) semiconductors requiring efficient heat dissipation and package performance, emphasis has been placed on the heat dissipation and reliability of chip-level packages [1–3]. WBG semiconductors can operate at considerably higher temperatures (> 250 °C) compared to conventional Si-based power devices (< 150 °C) [4]. To manage the high-temperature operation of SiC power devices, Ag sinter joining has emerged as a die attach material to Direct Bonded Copper (DBC) substrates, capable of withstanding harsh conditions, including temperatures exceeding 250 °C [5,6]. Ag paste sinter joining, using Ag nanoparticles (Ag nano-paste), has been developed for SiC power modules and demonstrates superior electrical and thermal conductivity after sintering [7–9]. The thermal conductivity can exceed 300 W/(m K), depending on the porosity of the sintered Ag [10–12]. Compared to traditional solder paste, Ag sinter paste also exhibits better initial bonding strength and higher temperature reliability [13–16].

Recently, to reduce the high material cost of Ag nanoparticles, Ag micro-sized particle paste (Ag micro-paste) or hybrid particle paste has been developed and demonstrated excellent thermal stability and thermal shock resistance properties [17–19]. However, both Ag nano-paste and Ag micro-paste still require organic solvents and a complex printing process. Additionally, Ag paste sinter joining is influenced by the solvent used and its evaporation, which usually takes >30 min for pressure-less sintering [20,21]. Although a preheating process for Ag paste promotes sol-

* Corresponding author.
E-mail address: chenchuantong@sanken.osaka-u.ac.jp (C. Chen).

https://doi.org/10.1016/j.jmst.2025.07.042

vent volatilization at low temperatures and shortens the sintering time, further organic solvent evaporation still requires a temperature exceeding the threshold for Ag particle necking growth, leading to prolonged sintering times [22,23]. To meet industrial demands and save time and cost, developing rapid bonding technologies that, like solder reflow, can be completed in just a few minutes is necessary [24–27].

Beyond die attach bonding, heat dissipation performance can be further enhanced by bonding the DBC substrate to an aluminum (Al) or copper (Cu) heatsink using high-thermal-conductivity materials. Current bonding techniques, including Pb-free solder, transient liquid phase (TLP) bonding, and thermal interface material (TIM) grease, exhibit high thermal resistance and compromise both heat dissipation and structural reliability [28]. SiC power modules utilizing Ag paste sinter joining for both die attach and substrate-heatsink bonding demonstrate remarkable heat dissipation, achieving 1.8 times lower thermal resistance than conventional solder and grease joint structures [29]. Although Ag paste sintering has been explored for both die attach and DBC-to-heatsink bonding, the process often involves multiple steps and prolonged sintering durations, especially for large-area bonding (e.g., 30 mm × 30 mm). Such processes risk incomplete solvent evaporation, resulting in interfacial voids, reduced bonding strength, and poor thermal dissipation [30].

On the other hand, solid-state bonding, which relies on atomic diffusion at temperatures around half the absolute melting point, has recently gained attention as an alternative to paste-based bonding [31–33]. Pure Ag sheets [34,35] and porous Ag sheets [36,37] have shown potential for low-temperature bonding (< 300 °C) without requiring organic solvents. In SiC packaging processes, solid-state bonding does not require complex printing processes like Ag paste sinter joining, improving packaging efficiency and reducing costs. Compared to bulk Ag sheet bonding, Ag porous sheet bonding can relieve interface stress with SiC, improving the reliability of SiC power devices in harsh environments. However, there are few reports on the simple preparation of uniform Ag porous sheets, especially large-area Ag porous sheets [38,39]. Furthermore, current solid-state bonding techniques still require high temperature and pressure over long durations (greater than 1 h) to achieve uniform bonding and interface diffusion [34–37]. Particularly for large-area solid-state bonding with pure metal, significant diffusion at the bonding interface requires extended processing times. Moreover, achieving a high interface bonding ratio remains a challenge, resulting in low initial bonding strength and poor interface reliability during high-temperature applications [38–40]. Developing a rapid solid-state bonding method with high thermal conductivity, short bonding times, and high bonding reliability remains a significant challenge, particularly for industrial-scale applications in SiC power modules.

This study proposes a novel approach to fabricating Ag porous sheets through hot-pressing of micro-sized Ag particles without organic solvents. By leveraging the high dislocation density and grain boundaries induced by ball milling, the resulting Ag porous sheets achieve rapid microstructural necking growth and high-density formation. A rapid solid-state bonding process based on these porous sheets is introduced, utilizing surface stress accumulation to enhance bonding efficiency. This method is evaluated for die attach bonding and large-area substrate-to-heatsink bonding (30 mm × 30 mm) under various conditions, including heating times (1–5 min) and temperatures (200–300 °C). Interface bonding quality, bonding strength, and the bonding mechanism are analyzed using SEM, XRD, TEM, EBSD, and 3D-finite element analysis (FEA). The proposed technique aims to address key limitations of existing methods, providing a scalable, cost-effective solution for high-performance SiC power module packaging.

2. Methodology

2.1. Ag porous sheet fabrication

In this study, Ag micron-sized flake particles with a median diameter range of 2.0–3.4 μm were utilized as the raw material. These particles were prepared through ball milling, which employs high-speed ball impact, as illustrated in Fig. 1(a). TEM observa-

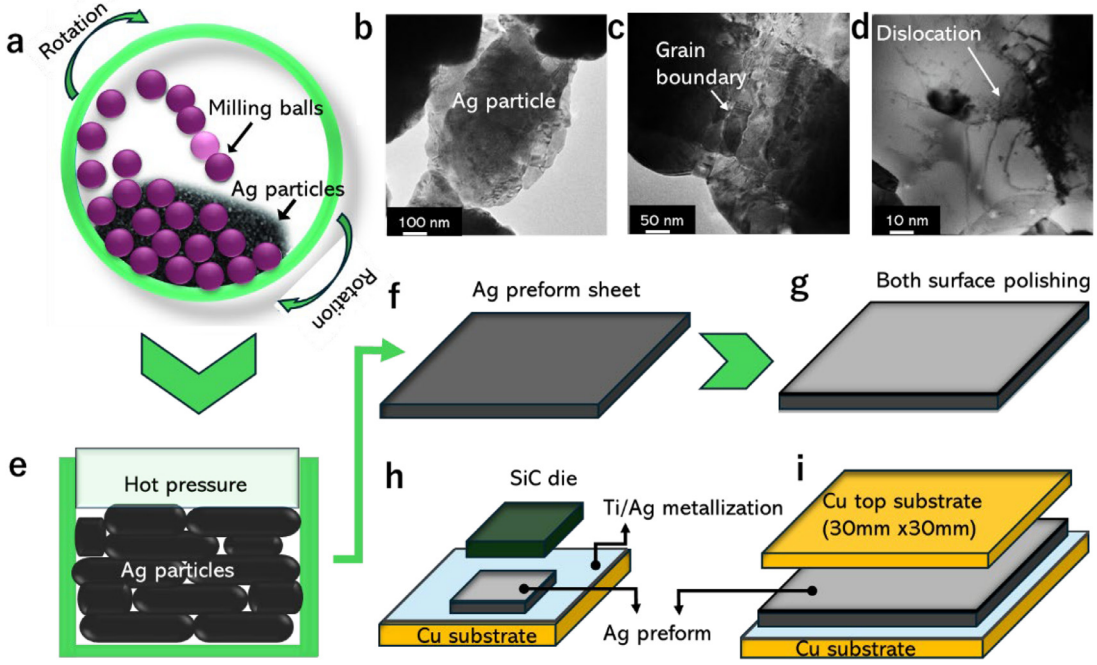

Fig. 1. (a) Micron-sized Ag flake particles with a ball milling process, (b) the TEM image of Ag flake particles, (c) the twin grain boundaries, (d) the dislocation in the Ag flake particle, (e) the image of hot pressure for the Ag flake particles, (f) the Ag porous sheet fabrication, (g) the surface polishing of Ag porous sheet, (h) SiC die bonding by Ag porous sheet, (i) large-area Cu substrate bonding by Ag porous sheet.

tions revealed the presence of numerous grain boundaries and dislocations within the Ag flake particles, as shown in Fig. 1(b–d). In our previous studies, it was suggested that grain boundaries act as sources for dislocation generation, while dislocations contribute to the low-temperature deformation of nanocrystalline materials [41,42]. Thus, the high density of grain boundaries and dislocations in the initial Ag flake particles likely facilitates grain structure deformation and residual strain development.

The preparation of large-area (30 mm × 30 mm) Ag porous sheets using these Ag micron-sized flake particles is schematically illustrated in Fig. 1(e). The Ag particles were placed into a square groove with a depth of 200 μm and subjected to a pressure of 20 MPa using a hot press at 300 °C for 3 min. During this process, the Ag particles underwent necking, forming a porous Ag sheet with dimensions of 30 mm × 30 mm and a thickness of approximately 100 μm.

Afterward, the Ag sheet was fixed onto a flat substrate using wax, and its surface was polished under pressure using an automated mechanical polisher. Initial polishing was performed with 1500- and 2000-grit SiC papers to achieve a nearly uniform surface on both sides. Subsequently, fine polishing was carried out using 4000-grit SiC papers to obtain the desired grain structure. The Ag sheet was then removed by heating, and the waxy residue was cleaned using acetone. An automated polishing process was employed to precisely control the sample thickness, reducing it to a consistent value of approximately 50 μm, as schematically illustrated in Fig. 1(g). The average surface roughness decreased from 228 nm before polishing to 40 nm after polishing. Following polishing, the microstructure of the Ag porous sheet exhibited an ultra-fine grain layer on the surface. This refined surface microstructure, which aids in achieving rapid interface bonding, will be further discussed in subsequent sections.

2.2. Die bonding and large-area substrate bonding

The dummy chips were composed of SiC with an area of 3 mm× 3 mm and a thickness of 0.4 mm. Cu substrates with dimensions of 10 mm× 10 mm and a thickness of 1 mm were also prepared. Both the SiC dummy chips and Cu substrates were coated with Ti/Ag layers (200 nm/1 μm) using a sputtering device (QAM-4C-SL). The Ag layer was applied to enhance interfacial bonding properties and prevent Cu diffusion. A schematic representation of the bonding structure between the SiC chip and Cu substrate, using an Ag porous sheet with a polished surface, is shown in Fig. 1(h). For this bonding process, the Ag porous sheet was cut to dimensions of 4 mm × 4 mm. Bonding was performed at different temperatures (200, 250, and 300 °C) and durations (1, 3, and 5 min) under a pressure of 20 MPa in air.

For large-area substrate bonding, bare Cu substrates with dimensions of 50 mm × 50 mm × 0.8 mm (length, width, and thickness) and Cu chips with dimensions of 30 mm × 30 mm × 0.8 mm were prepared. The Cu chips underwent a pretreatment cleaning process. Both bonding surfaces of the Cu chips and Cu substrates were sputtered with Ti/Ag layers (200 nm/1 μm) using the same sputtering device. A schematic diagram of the large-area bonding process using the Ag porous sheet is presented in Fig. 1(i). The Ag porous sheet was placed between the Cu chip and the Cu substrate, and the assembly was sintered at 250 °C for 3 min under a pressure of 20 MPa in air.

2.3. Characterization

The shear strength of the die-attached structure was measured using a shear test conducted with a die shear tester (DAGE, XD-7500) at a shear rate of 50 μm/s. The microstructure of the Ag porous sheet under different bonding temperatures and times was initially mechanically polished and subsequently fine-polished using an ion milling process (IM 4000, HITACHI). The surface morphologies, components, and structures of the sintered joint cross-section were observed using field-emission scanning electron microscopy (FE-SEM, Hitachi SU8020) equipped with energy-dispersive spectroscopy (EDS). Scanning acoustic tomography (SAT) was employed to examine the chip joint structure and large-area substrate joint structure under various bonding conditions. This analysis aimed to assess the interface bonding rate and the state of interface voids. To elucidate the solid-state bonding mechanism, the surface residual stress of the Ag porous sheet was measured before and after polishing, as well as before and after heating at different temperatures, using an X-ray residual stress measurement system (μ-X360 Ver. 3240). In this study, the cos-alpha (cos α) method evaluates residual stress by analyzing the distortion of Debye-Scherrer rings captured by a two-dimensional X-ray detector, with further confirmation provided by 3D finite element simulations. The crystallographic characteristics of the Ag porous sheet and bonding interface were quantitatively analyzed through electron backscatter diffraction (EBSD, Velocity Super, EDAX, USA). Additionally, the bonded interface between the SiC and Ag porous sheet at various bonding temperatures was investigated using transmission electron microscopy (TEM, JEM-ARM200F, JEOL).

3. Results and discussion

3.1. Ag porous sheet

Fig. 2(a) shows a photograph of the Ag porous sheet after surface polishing. No cracks or defects were observed on the surface, indicating that the Ag porous sheet can be fabricated with good uniformity over a large area. A magnified view of the surface is shown in Fig. 2(b), where fine Ag grains can be clearly observed. The grain structure of the polished surface was analyzed using EBSD, and the Inverse Pole Figure (IPF) image in Fig. 2(c) reveals that the grain orientation was random, with an average grain size of approximately 0.3 μm.

Fig. 2(d) depicts the cross-section of initial Ag particles before hot-pressing, and Fig. 2(e) shows the cross-section of the Ag porous sheet after the hot-pressing process, with the top surface polished. The Ag porous sheet formed by hot pressing, featuring both nano- and micro-pores. The porosity of the Ag porous sheet was approximately 12.2 %. Based on the relationship between porosity and thermal conductivity of porous Ag [43], the thermal conductivity of this sheet is estimated to be around 300 W/(m k). The microstructure, including the induced porosity and pore size, can be easily adjusted by modifying the temperature, time, and pressure during the hot-pressing process (see Fig. S1 in Supporting Information).

The top surface of the polished layer, shown in Fig. 2(f), exhibited a denser structure where the porosity decreased to about 3.7 %, approaching a bulk-like structure with a thickness of approximately 2 μm. This densification is likely due to the deformation of the Ag porous material during mechanical polishing, as large plastic deformation led to the observed reduction in porosity. Furthermore, it was evident that surface polishing reduced the grain size, forming an ultra-fine grain structure on the surface of the Ag porous sheet, where Ag resembles polycrystalline porous materials, as shown in Fig. 2(g, h).

3.2. SiC/Cu die-attached structure

To investigate the effects of bonding conditions on the structure and interface bonding, the evolution of the joint under different times and temperatures was observed. Cross-sectional images

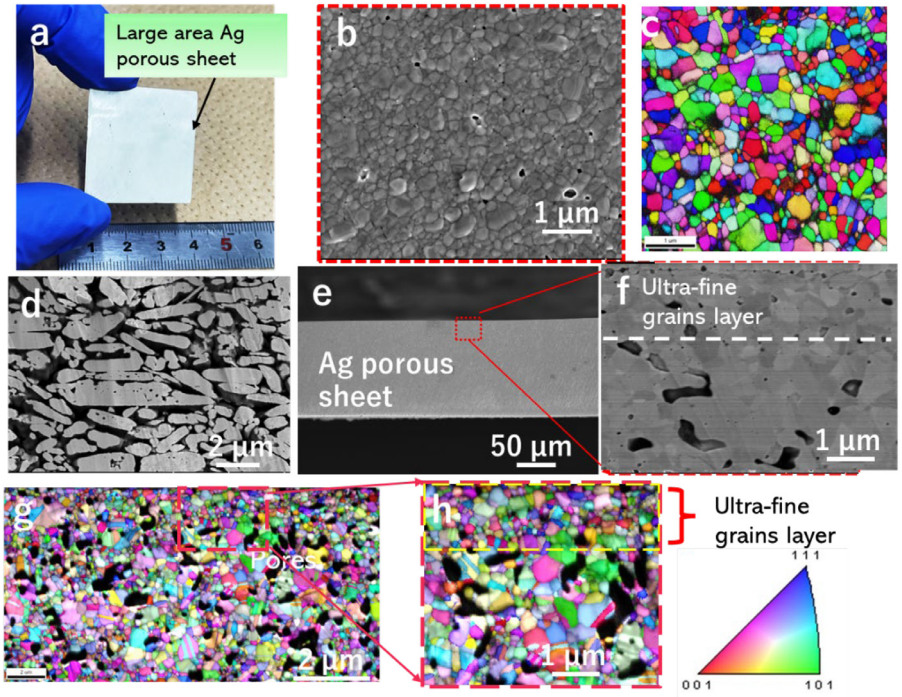

Fig. 2. (a) The photo of large area Ag porous sheet, (b) the SEM image of Ag porous sheet after polishing, (c) the grain structure of Ag porous sheet surface by EBSD analysis, (d) the cross section of Ag micro flake particle, (e) the cross section of Ag porous sheet, (f) the magnified view of Ag porous sheet at the polished surface, (g) the EBSD grain structure after surface polishing, (h) the magnified view of grains at the surface polished part.

of the Ag porous sheet SiC/Cu joints bonded for a short time of 1 min at 200, 250, and 300 °C are shown in Fig. 3. At 200 °C, the Ag porous sheet joints exhibited rapid bonding evolution, as shown in Fig. 3(a). While a rapid interface bonding process was achieved, some voids and cracks were observed at both the bonded interfaces with the SiC and Cu substrate, as illustrated in Fig. 3(b, c). At a heating temperature of 250 °C (Fig. 3(d)), some interface voids were still present at the bonded interface between the Ag porous sheet and SiC (Fig. 3(e)); however, no significant interface cracks were evident along the bonded line. Furthermore, the interface between the Ag porous sheet and Cu substrate exhibited good bonding quality, with no cracks or obvious voids, as shown in Fig. 3(f). The increase in temperature enhanced the interfacial bonding within the same bonding time. The longer bonding time can also improve the interfacial bonding at 250 °C (Fig. S2).

When the heating temperature was increased to 300 °C, as shown in Fig. 3(g), significant grain growth occurred between neighboring particles, leading to the formation of localized dense areas and robust interface bonding. The bonded interfaces between the Ag porous sheet and SiC, as well as between the Ag porous sheet and Cu substrate, are shown in Fig. 3(h) and Fig. 3(i), respectively. These interfaces became indistinguishable, indicating a high bonding strength. The microstructure at the interface was seamlessly connected to the Cu substrate without the generation of voids or cracks.

The bonded interface between the SiC and Ag porous sheet was examined using EBSD to analyze the grain structure of the Ag porous sheet and its influence on interfacial bonding behavior under different bonding conditions. Fig. 4(a, c, e, g) shows the EBSD analysis results for the high-magnification bonded interface between the SiC and Ag porous sheet under bonding conditions of 200 °C for 1 min, 250 °C for 1 min, 250 °C for 3 min, and 300 °C for 1 min, respectively. Corresponding inverse pole figure (IPF) maps of these regions are shown in Fig. 4(b, d, f, h), where areas with high-angle grain boundaries (HAGBs) and low-angle grain boundaries (LAGBs) are identified. The EBSD analysis results for the Ag porous sheet under different bonding conditions can be found in Fig. S3.

The EBSD results indicate that the grain orientation of the Ag porous sheet was randomly distributed, irrespective of bonding temperature or time. Additionally, the Ag sputtered layer exhibited a nano-twinned grain structure, with crystal grains growing in a columnar shape. In the cross-sectional direction, most grains were oriented in the [110] direction. Nano-twinned and columnar grain structures contribute to interfacial bonding under low-temperature and low-pressure conditions [44–47], and their formation is influenced by the Ag sputtering machine settings [47]. In this study, the Ag sputtering was performed using a direct current (DC) mode sputtering system with a deposition rate of 30 nm/min. The base pressure of the sputtering vacuum chamber was maintained at 5.0×10^{-3} Pa. Meanwhile, an ultra-fine grain layer structure was observed in the Ag porous sheet near the bonding line, which was denser than the grain structure farther from the bonding line for all the sintering conditions. This dense and fine-grained structure corresponds to the polished surface layer.

Under bonding conditions of 200 °C for 1 min, as shown in Fig. 4(a), a large gap is observed between the Ag sputtered layer and the Ag porous sheet, indicating insufficient interface diffusion. When the bonding temperature is increased to 250 °C for 1 min, interface bonding improves, although voids remain in some locations. With an extended bonding time of 3 min or an increased temperature of 300 °C, most grain particles join on the nanometer scale on both sides of the interface, as shown in Fig. 4(e, g), respectively.

These results demonstrate that pure metal Ag interfaces can achieve bonding in a very short time and at low temperatures. The physical mechanism of this interfacial bonding should be affected by the fine-grain layer that enhances interfacial diffusion [48,49], which will be discussed in detail later. From the IPF maps, large grains in the Ag porous sheet, far from the bonding line, often exhibit low-angle grain boundaries (LAGBs), as seen in Fig. 4(b, d). These large grains may have formed during the manufacturing

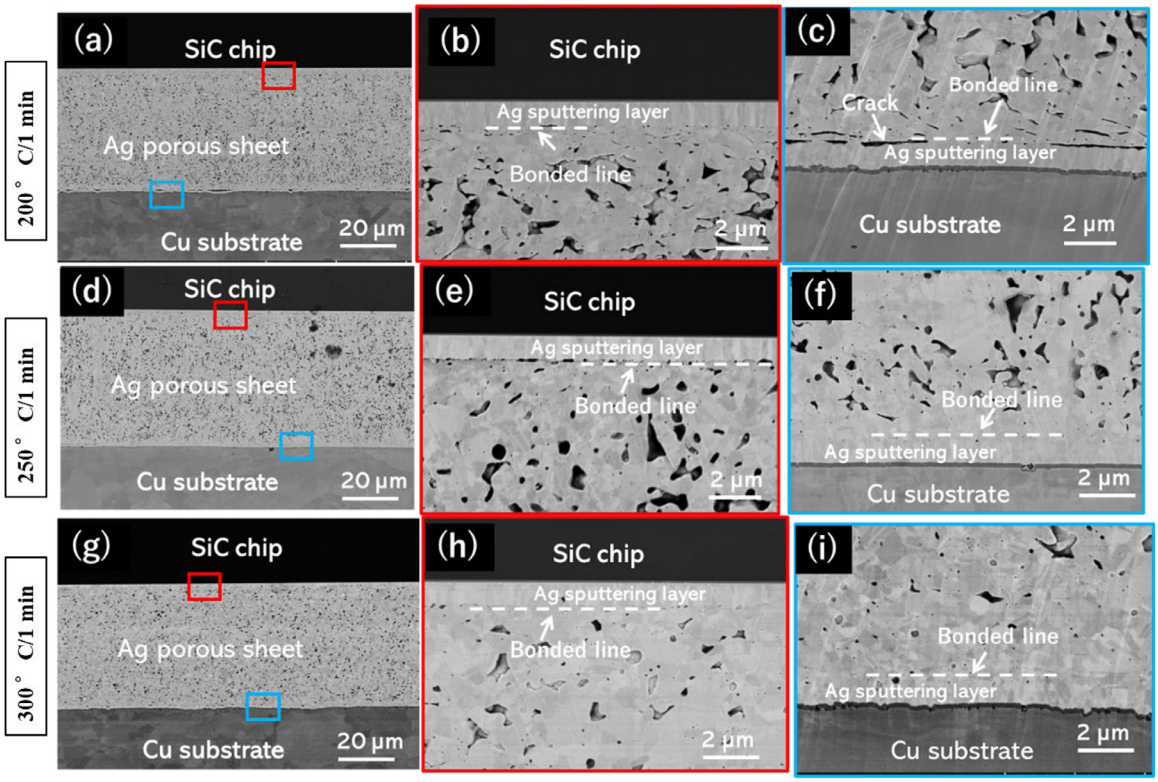

Fig. 3. Ag porous sheet joints obtained with a short bonding time of 1 min at (a) 200 °C, (d) 250 °C, and (g) 300 °C, the bonded interface between SiC chip and Ag porous sheet at (b) 200 °C, (e) 250 °C, and (h) 300 °C, the bonded interface between Ag porous sheet and Cu substrate at (c) 200 °C, (f) 250 °C, and (i) 300 °C.

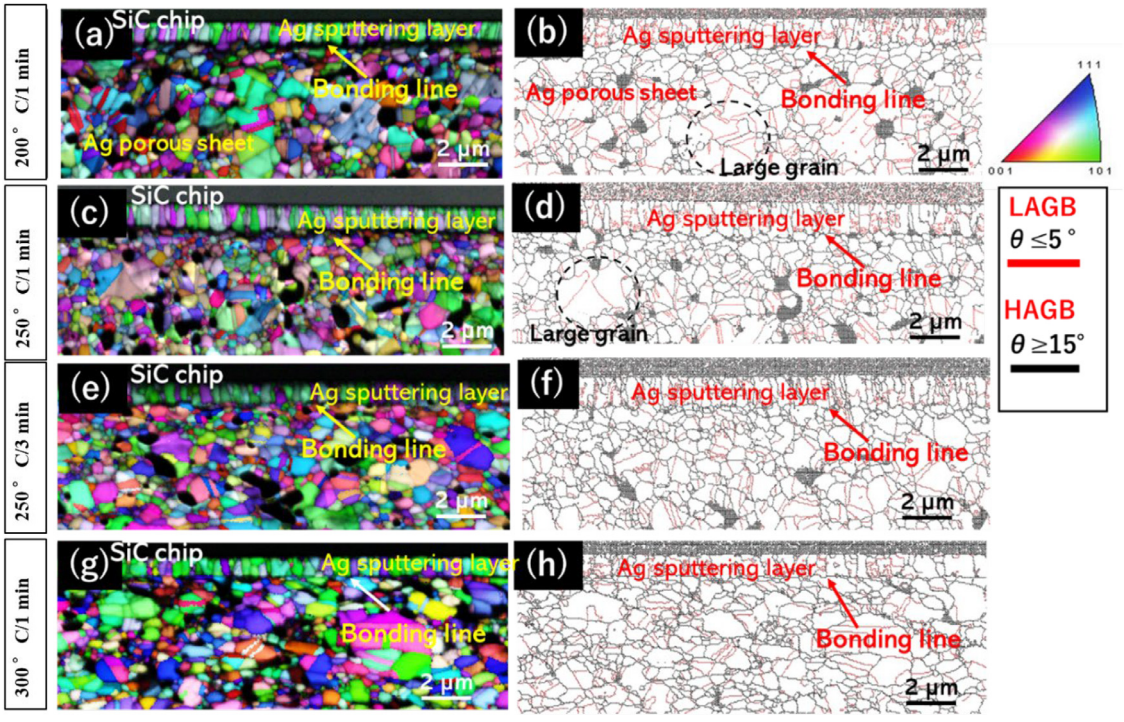

Fig. 4. (a, c, e, g) EBSD analysis results of the high magnified bonded interface between SiC and Ag porous sheet at the bonding condition of 200 °C for 1 min, 250 °C for 1 min, 250 °C for 3 min and 300 °C for 1 min, respectively; (b, d, f, h) the inverse pole figure (IPF) maps corresponding to the same location shown in (a, c, e, g), respectively.

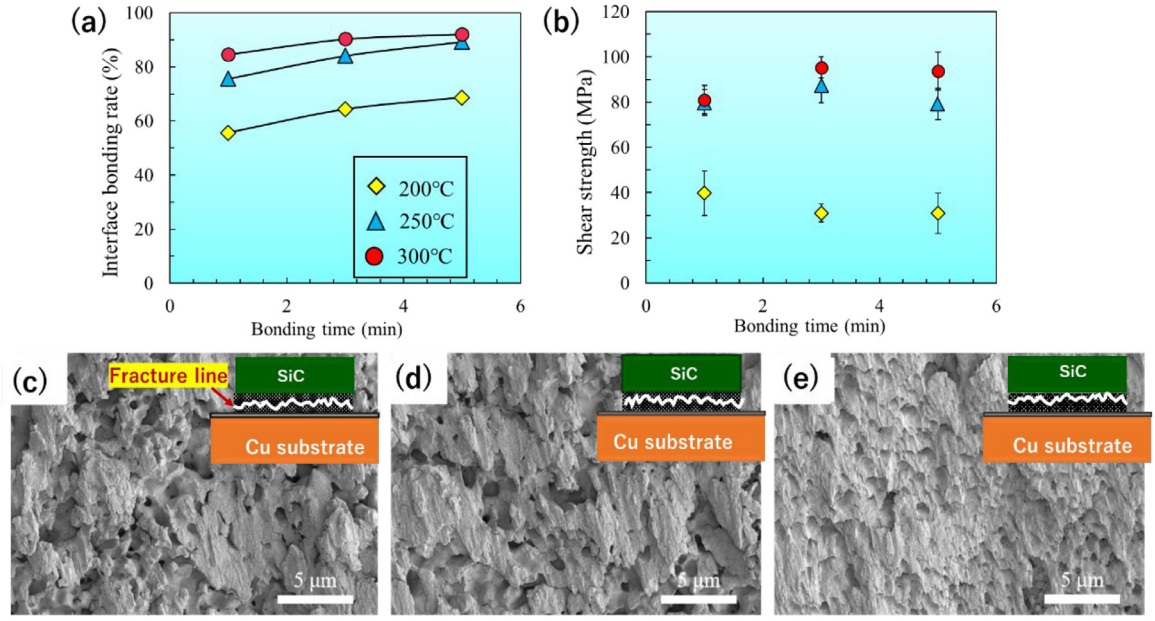

Fig. 5. (a) The interface bonding ratio between SiC and Ag porous sheet at the different bonding time and temperature, (b) the shear strength of joint structure at different sintering condition, fracture surfaces of Ag porous joints fabricated at 250 °C at bonding time of (c) 1, (d) 3, and (e) 5 min, respectively.

process of the Ag porous sheet, where the Ag flake particles undergo relatively rapid necking. In contrast, near the bonding line, high-angle grain boundaries (HAGBs) dominate. The presence of a polished layer near the bonding line suggests that the HAGBs are caused by significant plastic deformation during the polishing process.

The interface bonding ratio between the SiC and Ag porous sheet at different bonding times (1, 3, and 5 min) and temperatures (200, 250, and 300 °C) was investigated to understand the relationship between interface behaviors and bonding conditions. The interface bonding ratio represents the degree of connection at the interface between the Ag sputtering layer and the Ag porous sheet and is calculated using the following equation [50,51] based on SEM images:

$$\delta = \frac{\Sigma\, l_{\text{connected}}}{l_{\text{total}}} \tag{1}$$

where δ is the bonding ratio, l_{total} length of the interface, and $\Sigma l_{\text{connected}}$ is the total length of bonded locations between the interface.

In this study, SAT images of the joint structure under various bonding conditions were also referenced (Fig. S4). At 200 °C for 1 min, the interface bonding ratio reached 55.6 %, as shown in Fig. 5(a). When bonding times were extended to 3 min and 5 min at the same temperature, the interface bonding ratios increased to 64.3 % and 68.7 %, respectively. At 250 °C, the interface bonding ratio improved significantly, reaching 75.6 %, 84.1 %, and 89.3 % for bonding times of 1, 3, and 5 min, respectively. These values are higher than those achieved using Ag sinter paste on Ag metallization and Au substrates [50–52]. Additionally, the interface bonding ratio exceeded 90 % at a bonding temperature of 300 °C, which is markedly different from solder joints. In solder joints, the interface typically exhibits numerous Kirkendall voids during the reflow process [53,54].

The shear strength of the joint structure comprising SiC/Ag porous sheet/Cu substrate at different bonding temperatures and times is shown in Fig. 5(b). When bonding was performed at 200 °C for 1 min, the shear strength reached 39.7 MPa. The shear strength of the Ag porous sheet joint increased as the bonding temperature rose from 200 to 250 °C, which correlates with the interface bonding rate. At 250 °C, the joint strength achieved 79.8 MPa after a short bonding time of 1 min. Such a short processing time is advantageous for enhancing chip packaging efficiency.

Furthermore, extending the bonding time to 3 min at 250 °C significantly increased the shear strength to 87.4 MPa, a value notably higher than those reported for Ag sinter paste under slower sintering conditions [19,22,55–58]. The fracture surfaces of Ag porous joints bonded at 250 °C for 1, 3, and 5 min are shown in Fig. 5(c–e), respectively. Clear tensile deformation was observed in all joints. Notably, for the joint bonded for 5 min, the fracture surface exhibited a typical honeycomb-like plastic deformation pattern, indicating an elongation-to-failure process during fracture. These results demonstrate the high bonding capability of the Ag porous sheet, even with a short heating time of 1 min. Additionally, the fractures occurred within the Ag porous sheet layers, suggesting that the weakest region of the joint was the Ag porous sheet itself rather than the bonded interfaces.

3.3. Interface bonding mechanisms analysis

The interface bonding mechanism was analyzed and studied, and it was believed that the reason for the rapid interface bonding is affected by three factors: first, the nano-twinned and columnar crystal structure of the Ag sputtering layer; second, the surface ultra-fine grain structure of the Ag porous sheet; third, the surface stress caused by plastic deformation and grain structure changes. For the first factor, metal nano-twinned structures, such as those in Cu and Ag, have emerged as a promising method for electronic interconnections to improve the performance and durability of electronic devices [59–62]. The influence of the twin and columnar crystal structure of the Ag sputtering layer on low-temperature interface bonding has been confirmed in many studies [62–64].

On the other hand, in the process of solid low-temperature bonding for pure metals without intermetallic compound (IMC) growth, the most important parameter is the interface diffusion rate. The interface diffusion rate is mainly affected by the activation energy acting on the interface, which depends on external and internal parameters [65,66]. The external parameters, such as pressure, bonding temperature, and time applied to the interface, can

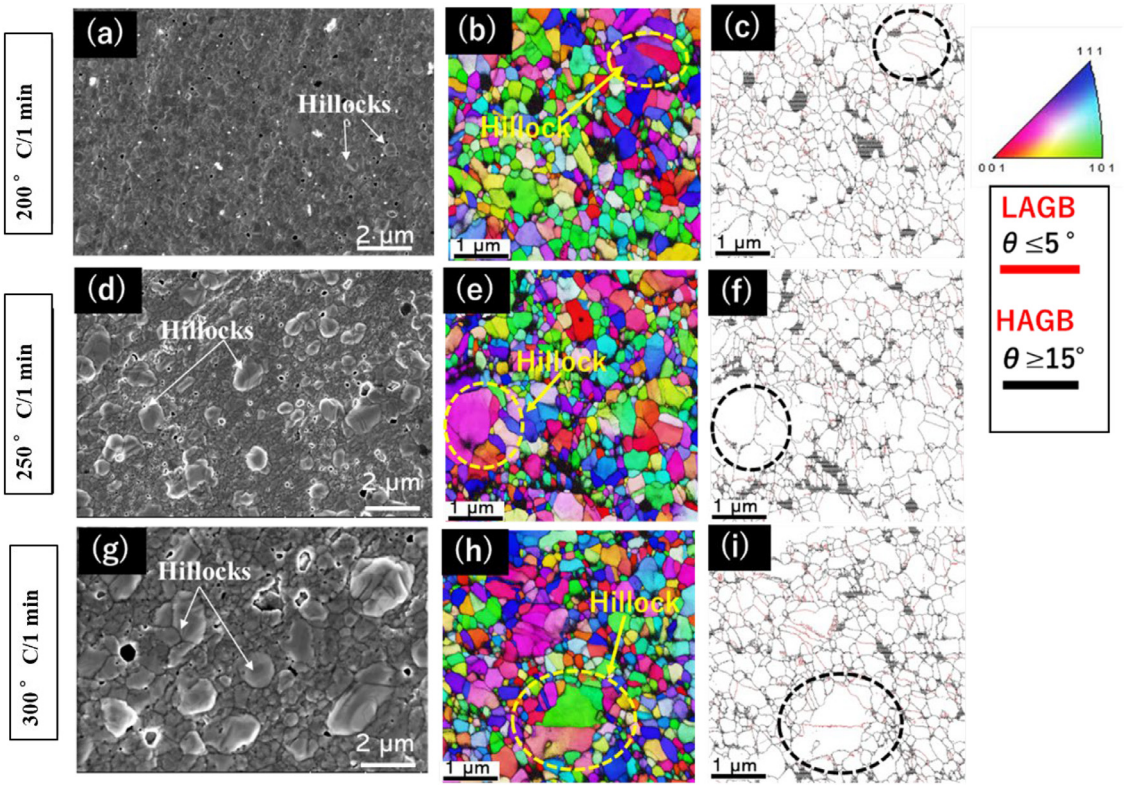

Fig. 6. (a–c) The SEM image, GB image and IPF image of the polished surface of Ag porous sheet after heating at 200 °C for 1 min, (d–f) after heating at 250 °C for 1 min, and (g–i) after heating at 300 °C for 1 min.

be varied during the bonding process. The diffusion coefficient (D) can be expressed as a function of the bonding temperature using the following equation [67,68]:

$$D = D_0 \exp^{(\frac{-Q}{Rt})} \tag{2}$$

where D_0 is the frequency pre-exponential, Q is the activation energy, R is the Boltzmann constant, and t is the temperature. Therefore, the higher temperature increases the interface diffusion, resulting in a good interface bonding rate and shear strength.

Internal parameters include the properties of the metal at the interface, grain size, grain boundary (GB) structure, and surface states such as plastic deformation and creep. According to the results of EBSD, the average grain size after polishing is 0.35 times that before surface polishing. Because there is an inverse relationship between the size of crystal particles and the density of GBs in the same volume, smaller grain sizes correspond to higher GB densities. In previous studies, it has been confirmed that temperature affects the growth rate mainly through the grain boundary mobility $m(T)$, which can be written as in Eq. (3) [69,70].

$$m(T) = \frac{m_0}{T} \exp\left(-\frac{Q_{mig}}{K_B T}\right) \tag{3}$$

where m_0 is a constant and Q_{mig} is an effective activation energy for boundary migration [71]. The value of Q_{mig} is usually found to be close to the grain boundary diffusion activation energy for grain growth in polycrystals. Therefore, in this study, the surface polishing of the Ag sheet surface leads to smaller grains and increased GB density, which in turn increases the interfacial diffusion.

On the other hand, the surface undergoes significant plastic deformation during the polishing process, corresponding to surface severe plastic deformation (SPD) mechanisms [72–75], where grain size changes through the sample depth, and gradient microstructures can, in some cases, be a superposition of different gradients. Significant plastic deformation leads to substantial residual stress accumulating on the surface. In previous studies, it was found that the stress on the Ag surface coated on Si would be released during the heating process, resulting in abnormal grain growth and eventually leading to hillock formation on the surface [43,44]. Abnormal grain growth has also been observed on cold-rolled Ag sheets and nano-gradient structures on Ag-plated substrates during heating [76,77]. This stress-driven abnormal grain growth accelerates bonding and diffusion between interfaces.

In this study, the Ag porous sheet after surface polishing was heated at 200, 250, and 300 °C for 1 min, and hillocks were indeed observed, as shown in Fig. 6(a), (d), and (g), respectively. At 200 °C, the average diameter of these hillocks was several hundred nanometers, increasing to over 1 μm at 300 °C. This confirmed that surface polishing induces residual stress, potentially contributing to rapid interface bonding. The grain structures of the surface after heating at 200, 250, and 300 °C are shown in Fig. 6(b, e, h), respectively. Notably, hillocks exhibit larger grain sizes compared with other Ag grains, indicating the presence of single or twin grain structures, as confirmed by the inverse pole figure (IPF) obtained through EBSD analysis. For the twin grain structures, hillocks display a LAGB structure, as shown in Fig. 6(c, f, i).

In addition, the surface residual stress of the Ag porous sheet before and after polishing was measured as shown in Fig. 7(a). The samples were prepared using the same hot-press process introduced in Section 2.1. Residual Stress of the Ag sheet surface before and after heating was measured by X-ray diffraction with the Cos-Alpha Method [78]. The measured Debye ring and the measurement conditions—including X-ray tube current (1.50 mA), tube voltage (30.00 kV), sample-to-detector distance (51.00 mm), X-ray incidence angle (35.0°), and X-ray wavelength (Kα, 2.229 Å, Cr)—were established for the analysis. Information on the test samples, the Debye ring for the sample before polishing, and the measurement conditions can be found in the Supporting Information (Fig. S5). In addition, the raw diffraction data (2θ shifts along α) are fit-

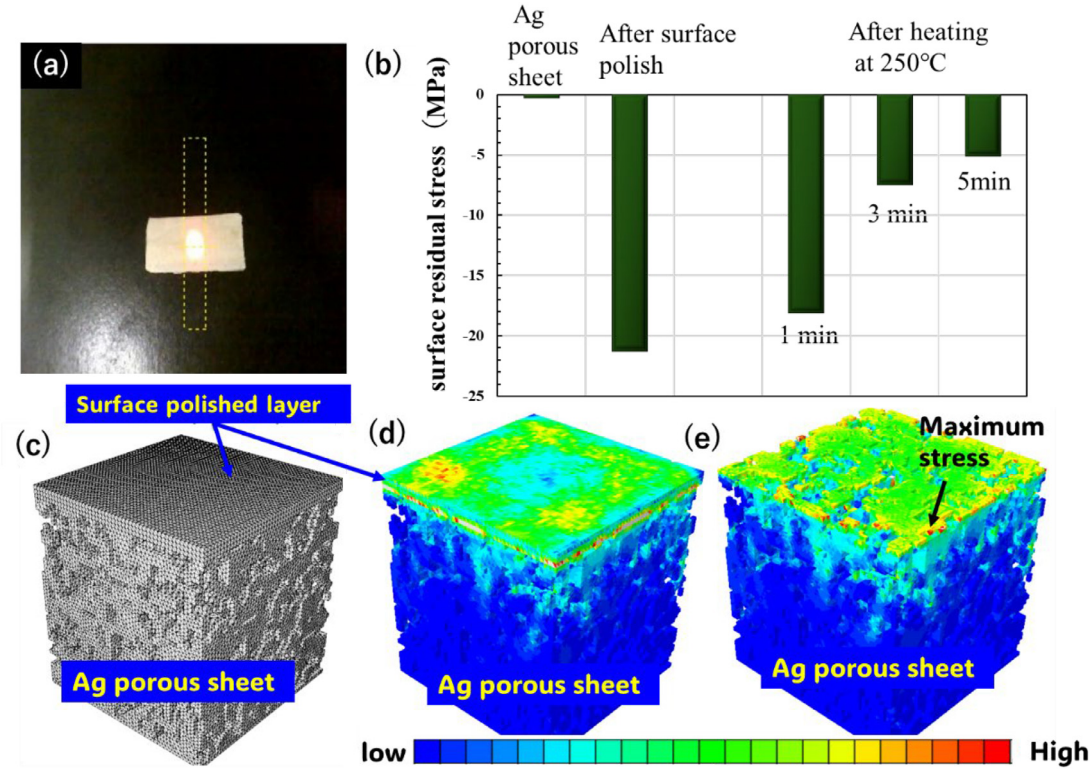

Fig. 7. (a) The sample for surface stress measurement, (b) the measured surface stress before and after surface polishing, and after heating with different time, (c) the 3D finite element simulation model for the surface polishing Ag porous sheet, (d) the Mises stress distribution on the surface polished Ag porous sheet at the heating temperature of 250 °C, and (e) Mises stress distribution on Ag porous sheet.

ted to determine the strain distribution. The strain is converted to stress using Hooke's law:

$$\sigma = \frac{E}{1+\nu} \times \epsilon \tag{4}$$

where E is Young's modulus, and ν is Poisson's ratio, ϵ is the strain. The value of E is 32 GPa and ν is 0.37 in this study [79].

No residual stress was detected before surface polishing. After surface polishing, residual compressive stress of −21.3 MPa was detected. This compressive stress acted as the driving force for abnormal grain growth. When the surface-polished Ag porous sheet was heated at 250 °C for 1, 3, and 5 min, the stress was released to −18.1, −7.49, and −5.12 MPa, respectively, as shown in Fig. 7(b). This indicates that as the heating time increases, the surface stress decreases progressively, and the released stress is converted into energy for abnormal grain growth on the surface and within the Ag porous sheet.

The compressive stress is related to surface plastic strain, which is induced not only by external stress but also by temperature and phase changes during polishing. This compressive stress, referred to as thermal stress (σ_{th}), is caused by mismatches in material properties (e.g., coefficient of thermal expansion (CTE), Young's modulus, and hardness) between the polished surface layer and the Ag porous sheet. The thermal stress (σ_{th}) is related to the temperature change (ΔT) as follows [80]:

$$\sigma_{th} = \frac{E_f}{1-\nu_f}(\alpha_s - \alpha_f)\Delta T \tag{5}$$

Here, E_f and ν_f represent the Young's modulus and Poisson's ratio of the film, respectively, while α_s and α_f denote the coefficients of thermal expansion (CTE) of the polished surface and the Ag porous sheet, respectively. ΔT is the temperature difference between the initial state and the heated state. In this study, the compressive stress in the surface-polished porous Ag structure was also confirmed through a 3D finite element simulation during the heating process. The 3D model was found by the 3D Gaussian Filtering Algorithm method, which applies a Gaussian function as a convolution kernel across all three spatial dimensions (*X*, *Y*, and *Z*) [81]. In the 3D model presented in Fig. 7(c), the polished surface, characterized by a dense layer, was assigned the same coefficient of thermal expansion (CTE) as bulk Ag (19.6 μm/(m K)). The CTE of the porous Ag sheet, along with other material properties such as elastic modulus and yield stress, was set to values determined experimentally at various temperatures in our recent study [82]. The Mises stress distribution within the model was analyzed during a temperature change from 25 to 250 °C, as illustrated in Fig. 7(d). Fig. 7(e) shows the stress distribution within the porous Ag structure, where the maximum stress of 17.6 MPa was observed at the interface with the polished layer. This stress acts as the driving force for hillock formation.

Furthermore, to investigate the interfacial microstructure of the bonded joints in more detail, TEM analysis was conducted on the interface between the Ag sputtered layer and the Ag porous sheet. TEM specimens were prepared using focused ion beam (FIB) techniques. Fig. 8(a) shows the interface bonded at 250 °C for 1 min. Most of the Ag sputtered layer exhibits a twin structure. Despite the low bonding temperature and short bonding time, the interface was almost fully bonded, with only a few interfacial voids observed. Fig. 8(b) presents the elemental mapping obtained by EDS analysis. Additionally, large grains were observed near the bonding interface between the Ag sputtered layer and the Ag porous sheet, suggesting interfacial diffusion and grain growth, as shown in Fig. 8(c, d).

When the bonding temperature increased to 300 °C for 1 min, the Ag interface exhibits a high-quality FCC single-crystal structure with a specific crystallographic orientation, as evidenced by the clear lattice fringes in the HRTEM image and FFT pattern, as

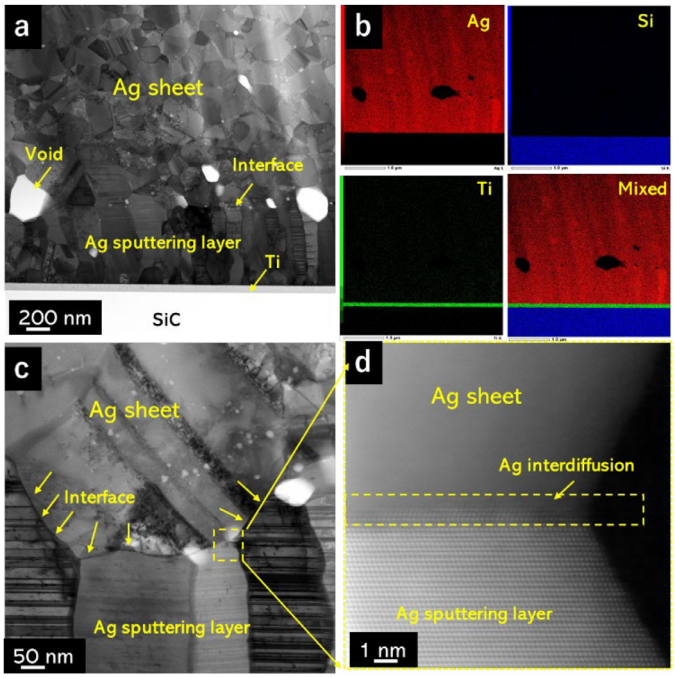

Fig. 8. (a) TEM image of Ag sputtering layer on SiC chip, interface between Ag sputtered layer and Ag porous sheet at bonding temperature of 250 °C for 1 min, (b) EDS element mapping, (c) the magnified view of bonded interface, and (d) the interface diffusion and interface formation.

shown in Fig. S6. The discrete diffraction spots suggest that the sample is oriented along a high-symmetry crystallographic zone axis, likely [100] or [110]. The large grains exhibit a single-crystal structure, corresponding to the abnormal grains observed on the surface of the Ag porous sheet in Fig. 6. Based on the experimental and simulation analyses, the abnormal grain growth is primarily attributed to surface-driven stress. Similarly, the interface formation and single-grain growth may also be predominantly caused by interfacial stress during such a short bonding time.

The rapid interface bonding mechanism of the Ag porous sheet is illustrated in Fig. 9. First, during hot pressing, Ag particles form a porous sheet in a short period without the need for additional solvents, as the particles bond together through neck formation. After surface polishing, the Ag porous sheet develops an ultra-fine-grained layer, as shown in Fig. 9(a), which possesses high surface energy and generates compressive residual stress due to changes in the grain structure. This compressive residual stress acts as the driving force for the formation of abnormal grains from the Ag grain boundaries on the surface during heating, as depicted in Fig. 9(b).

When the Ag porous sheet is bonded with SiC at a relatively low bonding temperature, the interface compressive stress is not fully released, leading to a slow growth rate of abnormal Ag grains. Additionally, insufficient interdiffusion at the interface results in the presence of voids and cracks, as shown in Fig. 9(c), leading to a low bonding rate. However, when the temperature increases to 250 °C, the abnormal Ag grains grow rapidly. With the accelerated interdiffusion at the interface, the bonding becomes complete. The abnormal Ag grains continue to grow, eventually forming a super-large single-crystal grain structure with the Ag sputtered layer, which enhances the bonding strength and solidifies the interface.

This bonding process and mechanism differ from traditional Ag paste sinter joining, which relies solely on interface interdiffusion to achieve bonding. The presence of interface-driven stress accelerates the diffusion process. Additionally, because no organic solvents are involved, there is no concern about solvent volatilization. Furthermore, this mechanism fundamentally differs from the traditional Transient Liquid Phase (TLP) bonding mechanism [83,84]. At this interface, only a single Ag element is present, and no intermetallic compounds (IMCs) are formed, which meets the high-temperature, high-thermal-conductivity, and high-reliability requirements of SiC die attachment.

3.4. Large area Cu–Cu bonding

After Cu–Cu bonding over an area of 30 mm ×30 mm using an Ag porous sheet at 250 °C for 3 min under an applied pres-

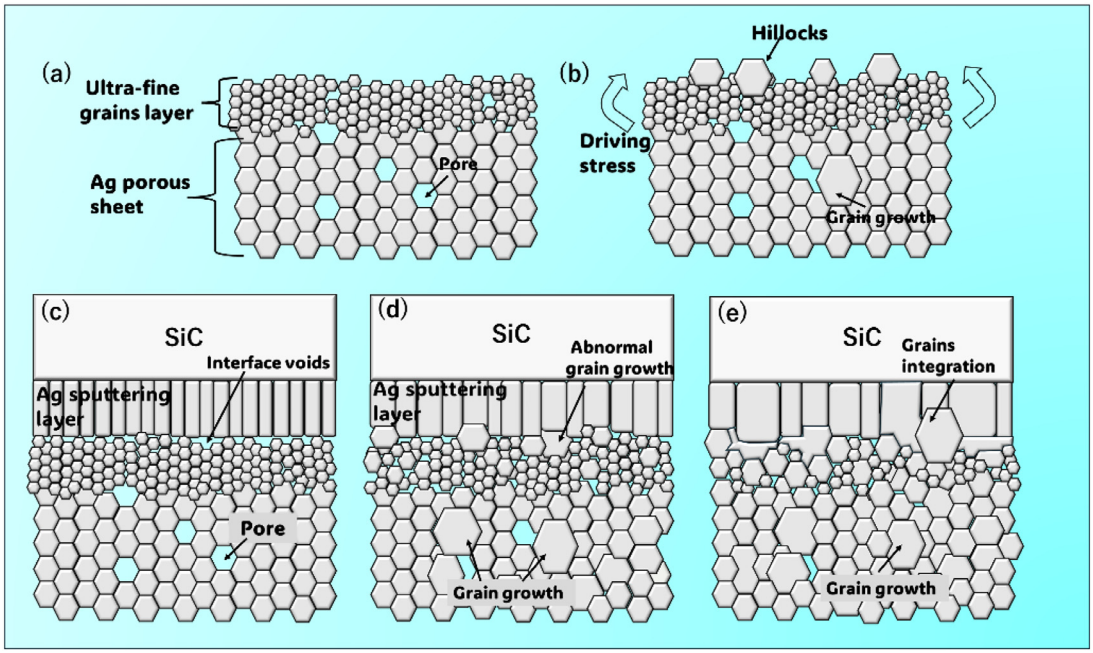

Fig. 9. (a) Schematic diagram of Ag porous sheet with ultra-fine grains layer, (b) the abnormal Ag grains grow caused by driving stress on the surface during heating process, (c) the joint structure with SiC at the bonded interface during a low temperature of 200 °C, (d) 250 °C, and (e) 300 °C.

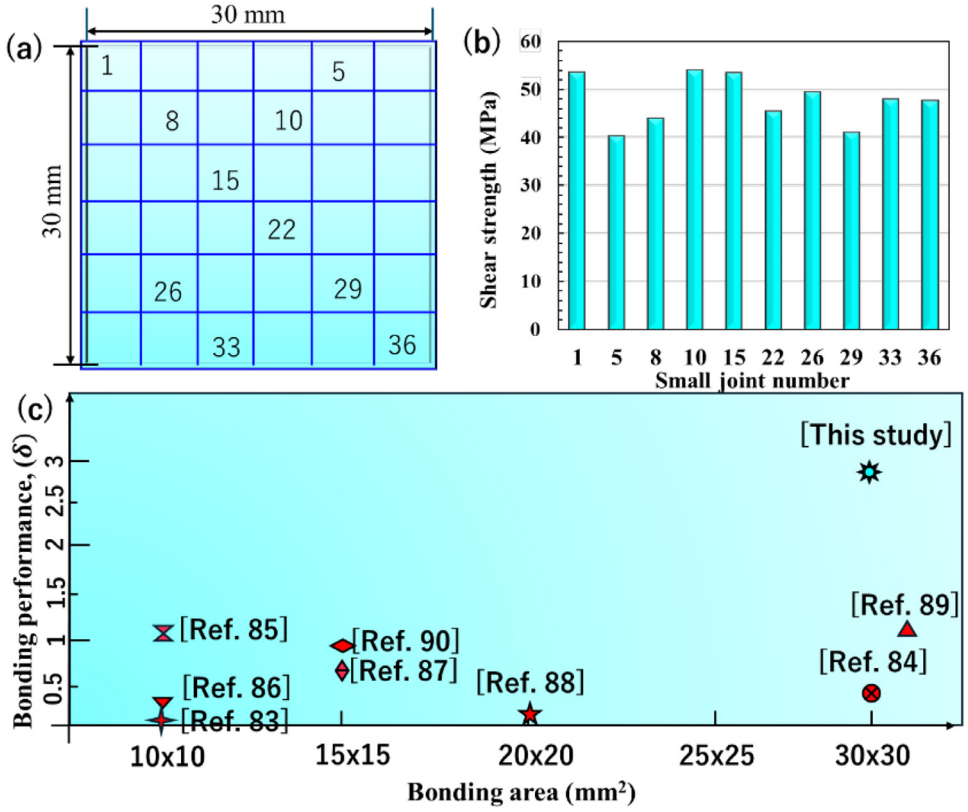

Fig. 10. (a) Schematic diagram of Cu−−Cu large area bonding with numbered small joint, (b) the shear strength of small joint, (c) the calculated bonding performance based on the recently reported large-area sintering studies.

sure of 20 MPa, the joint structure was sectioned into smaller pieces of 5 mm × 5 mm for shear strength measurement. Each small joint structure was numbered, as shown in Fig. 10(a), and the shear strength of several joints was measured, as illustrated in Fig. 10(b). The average shear strength calculated for these small joint structures was 47.9 MPa. The SAT image for the large area indicates that a good interface bonding ratio can be achieved using the Ag porous sheet (Fig. S7). In addition, cross-sectional micrographs of the large-area sintered joint are shown in Fig. S8. The Ag sheet was well bonded with no significant interfacial delamination across most of the bonding area, except for a small crack extending approximately 300 μm from the right edge, which disappears toward the center. The grain size and grain boundary characteristics were also similar to those observed in small die-size bonding. Considering that the side length of the Ag sheet used for bonding is 30 mm, the 300 μm crack corresponds to only 1/100 of the side length. While the presence of a crack in this localized edge area may affect interfacial reliability and thermal transport properties, its influence over the entire bonded region can be considered negligible.

The crack formation is likely due to the non-uniform thickness of the Ag sheet caused during the polishing process—particularly at the edges, which may be polished more than the central region, resulting in a thinner layer. This localized thinning could lead to interfacial cracking. However, the non-uniform thickness can be controlled and optimized in future processing.

To compare this method with Ag paste sinter joining for large areas, a new parameter was introduced to simplify the evaluation of sintered material performance in this study. In the case of Ag paste sinter joining, the bonding quality of the sintered joint is influenced by the sintering conditions, sintering area, and the intrinsic bonding performance of the sintered material. Generally, sintering temperature (T), time (t), and applied pressure (P) positively contribute to the bonding quality of the joint, representing the externally provided energy (E). The intrinsic bonding performance of the material during sintering is represented by material parameters (δ), which are positively correlated with the shear strength of the joint.

A good bonding material (δ) demonstrates characteristics such as rapid particle necking and interface necking, fast evaporation of organic solvents, minimal void generation, and other favorable properties. In this study, the externally provided energy during sintering is defined as the integration of applied pressure over time at a specific temperature, as expressed in Eq. (6).

$$E = \int T \times P \, \mathrm{d}t \tag{6}$$

The externally provided energy per unit area can be expressed using the following Eq. (7):

$$E_{(\mathrm{unit})} = \frac{E}{S} \tag{7}$$

There, $E_{(\mathrm{unit})}$ is the externally provided energy per unit area, and S is the bonding area. The joint quality (Q) after bonding should have a positively correlated relationship with $E_{(\mathrm{unit})}$ and performance of the bonding material (δ) as defined as the following Eq. (8). Then, the performance of the sinter material (δ) can be expressed as Eq. (9)

$$Q = \frac{E}{S} \times \delta \tag{8}$$

$$\delta = \frac{Q \times S}{E} \tag{9}$$

If the joint quality (Q) is equated to the shear strength of the joint, the performance of the bonding materials can be quantified numerically. In this study, units were omitted as defining precise

Table 1
The recently reported large-area sintering (≥ 10 mm × 10 mm) data with the calculated bonding performance for various bonding materials.

Bonding material	Sintering temperature, T (°C)	Sintering time, t (min)	Applied Pressure, P (MPa)	Bonding area, S (mm^2)	Shear strength, σ (MPa)	Bonding performance, δ
Cu nanopaste [83]	250	30	10	10 × 10	39.0	0.052
Cu nanopaste [83]	250	30	5	10 × 10	21.0	0.056
Cu nanopaste [83]	180	30	2	10 × 10	5.4	0.050
Cu-Ag paste [84]	300	90	5	30 × 30	31.9	0.212
Ag nanopaste [85]	250	10	1.77	10 × 10	50	1.129
Ag nanopaste [86]	275	20	5	10 × 10	31.6	0.114
Ag nanopaste [87]	300	30	1	15 × 15	29.8	0.745
Ag nanopaste [88]	180	120	5	20 × 20	12.5	0.227
Ag nanopaste [89]	275	60	2.8	41 × 23	59.3	1.21
Ag sheet film [90]	300	60	0.4	15 × 15	31.5	0.98
This study	250	3	20	30 × 30	47.9	2.874

physical units remains challenging. Based on the shear strength of Cu sinter paste for a 10 mm × 10 mm bonding area under various sintering temperatures, times, and pressures reported in a previous study [85], the calculated bonding performance is nearly identical, as shown in Table 1. This consistency indicates that the hypothesis is partially validated by reference data.

Furthermore, by comparing recently reported large-area sintering (≥ 10 mm × 10 mm) data with the calculated bonding performance, it is evident that the bonding performance of the Ag porous sheet significantly surpasses that of traditional Ag paste, Cu nanopaste, and Cu-Ag mixed sinter paste joining. The detailed results are presented in Fig. 10(c) and Table 1 [85–92].

4. Conclusions

A rapid solid-state bonding technology was achieved using an Ag porous sheet with a surface ultra-fine-grained layer. The shear strength of the joint structure reached 82.1 MPa at a bonding temperature of 250 °C in just 1 min. This rapid and compact interface formation is attributed to the exceptional bonding characteristics introduced by the Ag porous sheet. The ultra-fine-grained structure on the surface of the Ag porous sheet, along with the formation of compressive residual stress, significantly accelerated Ag diffusion and promoted hillock generation. These factors greatly enhanced the bonding capability between the SiC and Cu substrate within a short timeframe. Furthermore, for Cu–Cu bonding over an area of 30 mm × 30 mm using this Ag porous sheet at 250 °C for 3 min, the average shear strength of the joint structures was 47.9 MPa. A comparison with recently reported large-area sintering data reveals that the bonding performance of the Ag porous sheet significantly exceeds that of traditional Ag paste, Cu nanopaste, and other bonding materials. In addition, the sheet bonding process eliminates the need for paste printing and avoids storage-related issues associated with solvent-based materials. The adoption of this Ag porous sheet offers a highly efficient bonding process, making it highly suitable for a wide range of applications in high-temperature and high-power electronics.

Declaration of competing interest

The authors declare that they have no known competing financial interests or personal relationships that could have appeared to influence the work reported in this paper.

CRediT authorship contribution statement

Chuantong Chen: Writing – review & editing, Writing – original draft, Supervision, Methodology, Funding acquisition. **Luobin Zhang:** Investigation, Data curation. **Fupeng Huo:** Resources, Methodology, Investigation, Data curation. **Minoru Ueshima:** Project administration, Methodology, Investigation. **Yutai Su:** Methodology, Investigation, Formal analysis, Data curation. **Xu Long:** Methodology, Investigation, Conceptualization. **Koji S Nakayama:** Resources, Methodology, Conceptualization. **Masahiko Nishijima:** Methodology, Investigation, Data curation. **Hiroaki Miyake:** Methodology, Investigation, Formal analysis, Conceptualization. **Mingyu Li:** Validation, Methodology, Investigation. **Katsuaki Suganuma:** Visualization, Supervision.

Acknowledgements

This work was supported by a project (JPNP14004, No. 21502156-0) commissioned by the New Energy and Industrial Technology Development Organization (NEDO) and JSPS KAKENHI (No. 22K04243), and JST (No. JPMJSF23DB).

Supplementary materials

Supplementary material associated with this article can be found, in the online version, at doi:10.1016/j.jmst.2025.07.042.

References

[1] L. Zhang, X. Yuan, X. Wu, C. Shi, J. Zhang, Y. Zhang, IEEE Trans. Power Electron. 34 (2019) 1181–1196.
[2] H. Sakairi, T. Yanagi, H. Otake, N. Kuroda, H. Tanigawa, IEEE Trans. Power Electron. 33 (2018) 7314–7325.
[3] J. Millan, P. Godignon, X. Perpina, A. Perez-Tomas, J. Rebollo, IEEE Trans. Power Electron. 29 (2014) 2155–2163.
[4] P. Ning, F. Wang, K.D.T. Ngo, IEEE Trans. Power Electron. 26 (2011) 3079–3083.
[5] S.A. Paknejad, S.H. Mannan, Microelectron. Rel. 70 (2017) 1–11.
[6] S. Xi, X. Shen, J. Li, Mater. Sci. Eng. B 317 (2025) 118220.
[7] H. Zheng, D. Berry, K.D.T. Ngo, G.-Q. Lu, IEEE Trans. Compon. Packag. Manuf. Technol. 4 (2014) 377–384.
[8] S. Fu, Y. Mei, X. Li, C. Ma, G.-Q. Lu, IEEE Trans. Power Electron. 32 (2017) 6049–6058.
[9] H.–.Q. Zhang, H.–.L. Bai, Q. Jia, W. Guo, L. Liu, G.-S. Zou, Acta Metall.-Sin.-Engl. Lett. 33 (2020) 1543–1555.
[10] C. Du, G. Zou, J. Huo, B. Feng, Z. A, L. Liu, J. Mater. Sci. 58 (2023) 16160–16171.
[11] C. Du, G. Zou, B. Feng, J. Huo, A. Z, Y. Xiao, W. Wang, L. Liu, J. Electron. Mater. 52 (2023) 2347–2358.
[12] T. Matsuda, R. Seo, A. Takeuchi, K. Uesugi, M. Yasutake, M. Kambara, A. Hirose, Mater. Sci. Eng. A 923 (2025) 147692.
[13] Z. Zhang, C. Chen, A. Suetake, M.C. Hsieh, W. Li, N. Wakasugi, K. Takeshita, Y. Yamaguchi, Y. Momose, K. Suganuma, J. Electron. Mater. 50 (2021) 6597–6606.
[14] D. Kim, S. Nagao, C. Chen, N. Wakasugi, Y. Yamamoto, A. Suetake, H. Pan, M. Lu, H. Ji, IEEE Trans. Power Electron. 36 (2021) 4977–4990.
[15] D. Kim, C. Chen, S. Nagao, K. Suganuma, J. Mater. Sci.: Mater. Electron. 31 (2020) 587–598.
[16] J. Dai, J. Li, P. Agyakwa, M. Corfield, C.M. Johnson, IEEE Trans. Device Mater. Reliab. 18 (2018) 256–265.
[17] C. Chen, C. Choe, Z. Zhang, D. Kim, K. Suganuma, J. Mater. Sci.: Mater. Electron. 29 (2018) 14335–14346.
[18] C. Chen, Z. Zhang, Q. Wang, B. Zhang, Y. Gao, T. Sasamura, Y. Oda, N. Ma, K. Suganuma, J. Alloy. Compd. 828 (2020) 154397.
[19] K.S. Siow, J. Electron. Mater. 43 (2014) 947–961.
[20] M. Wang, Y. Mei, X. Li, R. Burgos, D. Boroyevich, G.-Q. Lu, IEEE Trans. Power Electron. 34 (2019) 7121–7125.

[21] M. Wang, Y. Mei, W. Hu, X. Li, G.-Q. Lu, IEEE J. Electron. Mater. Sel. Top. P. 10 (2022) 2645–2655.
[22] T. Chen, K. Siow, J. Alloy. Compd. 866 (2021) 158783.
[23] M. Calabretta, A. Sitta, S. Massimo, G. Sequenzia, Appl. Sci. 11 (2021) 7012.
[24] M.I. Kim, E.B. Choi, J.-H. Lee, J. Mater. Res. Technol. 9 (2020) 16006–1617.
[25] M.I. Kim, J.-H. Lee, J. Mater. Res. Technol. 9 (2021) 1724–1738.
[26] E.B. Choi, Y.-J. Lee, J.-H. Lee, J. Alloy. Compd. 897 (2022) 163223.
[27] E.B. Choi, J.-H. Lee, Appl. Surf. Sci. 580 (2022) 152347.
[28] W. Xing, Y. Xu, C. Song, T. Deng, Nanomaterials 12 (2022) 3365.
[29] C. Chen, A. Suetake, F. Huo, D. Kim, Z. Zhang, M.C. Hsieh, W. Li, N. Wakasugi, K. Takeshita, Y. Yamaguchi, Y. Momose, K. Suganuma, IEEE Trans. Power Electron. 39 (2024) 10638–10650.
[30] B. Zhang, C. Chen, T. Sekiguchi, Y. Liu, C. Li, K. Suganuma, J. Mater. Sci. Technol. 113 (2022) 261–270.
[31] S. Schumacher, R. Birringer, R. Strauß, H. Gleiter, Acta Metall. 37 (1989) 2485–2488.
[32] R. Würschum, S. Herth, U. Brossmann, Mater. Sci. Eng. A 5 (2003) 365–372.
[33] T. Shimatsu, M. Uomoto, J. Vac. Sci. Technol. B 28 (2010) 706–714.
[34] S. Noh, C. Choe, C. Chen, K. Suganuma, Appl. Phys. Express 11 (2017) 016501.
[35] C. Oh, S. Nagao, T. Kunimune, K. Suganuma, Appl. Phys. Lett. 104 (2014) 161603.
[36] C. Chen, S. Noh, H. Zhang, C. Choe, J. Jiu, S. Nagao, K. Suganuma, Scr. Mater. 146 (2018) 123–127.
[37] E. Jo, Y.R. Kim, S. Lee, N. Masahiko, C. Chen, K. Suganuma, Y.B. Park, D. Kim, Mater. Lett. 378 (2015) 137633.
[38] C. Chen, K. Suganuma, J. Mater. Sci.-Mater. Electron. 29 (2018) 13418–13428.
[39] M. Kim, H. Nishikawa, Scr. Mater. 92 (2014) 43–46.
[40] W. Wang, G. Zou, Q. Jia, H. Zhang, B. Feng, Z. Deng, L. Liu, Mater. Sci. Eng. A 793 (2020) 139894.
[41] C. Chen, K. Suganuma, Mater. Des. 162 (2019) 311–321.
[42] J. Yeom, S. Nagao, C. Chen, T. Sugahara, H. Zhang, C. Choe, Appl. Phys. Lett. 114 (2019) 253103.
[43] J. Liang, H.-K. Yang, X. Huang, L.-Y. Gao, Z.-Q. Liu, Materials 18 (2025) 1435.
[44] T. Kunimune, M. Kuramoto, S. Ogawa, T. Sugahara, S. Nagao, K. Suganuma, Acta Mater. 89 (2015) 133–140.
[45] C. Oh, S. Nagao, K. Suganuma, J. Electron. Mater. 43 (2014) 4406–4412.
[46] Y.C. Lai, Z.H. Yang, Y.H. Chen, A. Lin, T. Chuang, J. Mater. Eng. Perform. 33 (2024) 8044–8056.
[47] D. Lu, X. Wang, H. Pan, X. Zheng, M. Li, H. Ji, IEEE Trans. Power Electron. 39 (2024) 6040–6051.
[48] R.K. Koju, Y. Mishin, Acta Mater. 198 (2020) 111–120.
[49] J. Jaseliunaite, A. Galdikas, Materials 13 (2020) 1051.
[50] L. Mikutta, F. Otto, J. Schadewald, Microelectron. Rel. 168 (2025) 115691.
[51] D. Kim, M. Kim, Mater. Charact. 198 (2023) 112758.
[52] C. Chen, K. Suganuma, T. Iwashige, K. Sugiura, K. Tsuruta, J. Mater. Sci.: Mater. Electron. 29 (2018) 1785–1797.
[53] J. Wang, J. Chen, L. Zhang, Z. Zhang, Y. Han, X. Hu, H. Lu, J. Adv. Join. Process. 6 (2022) 100125.
[54] K. Suganuma, S. Sakamoto, N. Kagami, D. Wakuda, K.-S. Kim, M. Nogi, Microelectron. Rel. 52 (2012) 375–380.
[55] H. Nishikawa, X. Liu, X. Wang, A. Fujita, N. Kamada, M. Saito, Mater. Lett. 161 (2015) 231–233.
[56] S.A. Paknejad, G. Dumas, G. West, G. Lewis, S.H. Mannan, J. Alloy. Compd. 617 (2014) 994–1001.
[57] M. Li, S. Huang, Z. Ding, C. Li, J. Electron. Mater. 54 (2025) 6054–6068.
[58] L. Chang, J. Wang, F. Ouyang, Mater. Chem. Phys. 274 (2021) 125159.
[59] S. Chang, Y. Chu, K.N. Tu, C. Chen, Mater. Sci. Eng. A 804 (2021) 140754.
[60] F. Shen, C. Huang, H. Lo, W. Hsu, C. Wang, C. Chen, W. Wu, Acta Mater. 219 (2021) 117250.
[61] D. Lu, H. Pan, X. Wang, Y. Zhong, R. Shi, H. Ji, Mater. Des. 240 (2024) 112839.
[62] M. Zhang, L. Gao, J. Li, R. Sun, Z. Liu, Mater. Chem. Phys. 306 (2023) 128089.
[63] P.F. Lin, D.P. Tran, H.C. Liu, Y.Y. Li, C. Chen, Materials 15 (2022) 937.
[64] K. Teigen, X. Li, J. Lowengrub, F. Wang, A. Voigt, Commun. Math. Sci. 4 (2009) 1009–1037.
[65] D. Amram, L. Klinger, N. Gazit, H. Gluska, E. Rabkin, Acta Mater. 69 (2014) 386–396.
[66] E.A. Brandes, Gold Bull. 8 (1975) 41–47.
[67] J. Wang, Y. Li, W. Huang, React. Kinet. Mech. Catal. 95 (2008) 71–79.
[68] C.E. Krill III, L. Helfen, D. Michels, H. Natter, A. Fitch, O. Masson, R. Birringer, Phys. Rev. Lett. 86 (2001) 842.
[69] A. Michels, C.E. Krill, H. Ehrhardt, R. Birringer, D.T. Wu, Acta Mater. 47 (1999) 2143–2152.
[70] L.C. Chen, F. Spaepen, J. Appl. Phys. 69 (1991) 679–688.
[71] M. Sato, N. Tsuji, Y. Minamino, Y. Koizumi, Sci. Technol. Adv. Mater. 5 (2004) 145.
[72] J. Hong, H. Park, J. Kim, M. Seok, H. Choi, Y. Kwon, D. Lee, J. Mater. Res. Technol. 24 (2023) 7076–7090.
[73] J. Yan, Nanomaterials 11 (2021) 927.
[74] D. Raabe, M. Sachtleber, H. Weiland, G. Scheele, Z. Zhao, Acta Mater. 51 (2003) 1539–1560.
[75] T. Grosdidier, M. Novelli, L. Weiss, Mater. Trans. 64 (2023) 1695–1708.
[76] S. Noh, H. Zhang, J. Yeom, C. Chen, C. Li, K. Suganuma, Microelectron. Rel. (2018) 701–706 88–90.
[77] B. Zhang, Z. Zhao, Y. Liu, H. Ma, C. Shi, Y.-H. Mei, IEEE Trans. Compon. Packag. Manuf. Technol. 14 (2024) 1156–1163.
[78] Y. Lu, Y. Li, M. Saka, Appl. Surf. Sci. 351 (2015) 1011–1015.
[79] C. Chen, S. Nagao, H. Zhang, J. Jiu, T. Sugahara, K. Suganuma, T. Iwashige, J. Electron. Mater. 46 (2017) 1576–1586.
[80] A.G. Blachman, Metall. Trans. 236 (1971) 699–709.
[81] Y. Su, Z. Shen, X. Long, C. Chen, L. Qi, X. Chao, Mater. Sci. Eng. A 872 (2023) 145001.
[82] Y. Liu, C. Chen, Y. Wang, Z. Zhang, R. Liu, M. Ueshima, I. Ota, H. Nishikawa, M. Nishijima, K.S. Nakayama, K. Suganuma, Compos. Part B-Eng. 281 (2024) 111519.
[83] G.O. Cook, C.D. Sorensen, J. Mater. Sci. 46 (2011) 5305–5323.
[84] L. Sun, L. Zhang, C. Wei, M. Chen, Y. Zhang, J. Mater. Process. Technol. 307 (2022) 117686.
[85] W.Y. Li, C.T. Chen, M. Ueshima, T. Kobatake, K. Suganuma, Microelectron. Reliab. 150 (2023) 115105.
[86] C. Chen, S. Zhao, T. Sekiguchi, K. Suganuma, J. Sci.-Adv. Mater. Devices 8 (2023) 100606.
[87] S. Fu, Y. Mei, G. Lu, X. Li, G. Chen, X. Chen, Mater. Lett. 128 (2014) 42–45.
[88] G. Lei, J.N. Calata, G.-Q. Lu, X. Chen, S. Luo, IEEE Trans. Compon. Packag. Technol. 33 (2010) 98–104.
[89] B. Zhang, X. Lu, Y. Xie, Z. Hou, W. Pan, Y.-H. Mei, In: Proc. 2024 25th Int. Conf. Electron. Packag. Technol. (ICEPT), Tianjin, China, 2024, pp. 1–5.
[90] S. Chen, Y.-H. Mei, M. Wang, X. Li, G.-Q. Lu, IEEE Trans. Compon. Packag. Manuf. Technol. 12 (2022) 707–710.
[91] Y.-S. Tan, X. Li, X. Chen, G.-Q. Lu, Y.-H. Mei, IEEE Trans. Compon. Packag. Manuf. Technol. 8 (2018) 202–209.
[92] C. Chen, D. Kim, Z. Wang, Z. Zhang, Y. Gao, C. Choe, K. Suganuma, Ceram. Int. 45 (2019) 9573–9579.